FLAP EFFICIENCY VERSUS FLAP HEATING OF A WINGED REENTRY VEHICLE - A CHALLENGE FOR THE CFD -

J.M.A. Longo and R. Radespiel

DLR - Braunschweig
Institut for Design Aerodynamic
Lilienthalplatz 7,D-38108 Braunschweig, Fed. Rep. Germany
(Telephone +49/531-295 2833 , Telefax +49/531-295 2320)

Abstract

In the present study Navier-Stokes solutions are analysed for a winged reentry vehicle at hypersonic free stream conditions corresponding to both, cold wind tunnel tests and a flight trajectory point. The flow was computed as laminar, assuming calorically perfect gas for the wind tunnel case. The high-temperature effects on thermodynamic and transport properties are modelled by assuming air in thermochemical equilibrium. Computations are presented for two types of control surfaces geometry: cambered and plain, for clean configurations and for configurations with deflected control surfaces. The accuracy of the computed solutions is addressed by grid refinement studies and by comparing numerical results with available experimental data. Also the importance of the viscous effects is shown by comparing the Navier-Stokes solutions with Euler solutions.

1. Introduction

The European spaceplane HERMES is a 15.5 meter long vehicle of the so-called class "winged reentry vehicle (RV)". By design it is completely located within the forebody bow shock. The flight envelope of HERMES comprises different aerodynamic domains[1] (Fig.1): rarefied gas, hot and cold hypersonic flow, supersonic and subsonic flow. Along the reentry trajectory, the HERMES vehicle should fly over an angle of attack range from about 50° to zero degree, during which a reaction control systen (RCS) is used in combination with aerodynamic surfaces to achieve longitudinal and lateral control. The initial entry phase extends to an altitude approximately 75km during which the longitudinal control provided by the RCS should blend with the surface controls, the latter gaining in effectiveness as the dynamic pressure increases. The aerodynamic surface controls of HERMES (Fig.2) include elevons, winglets with rudders and a hinged body flap located at the lower aft end of the fuselage to augment control during descent and landing approach. Short reentry vehicles like HERMES exhibit large heat loads which put constrains on the maximum deflection angle of the control surfaces in order to maintain acceptable structural temperatures under entry heating environment.

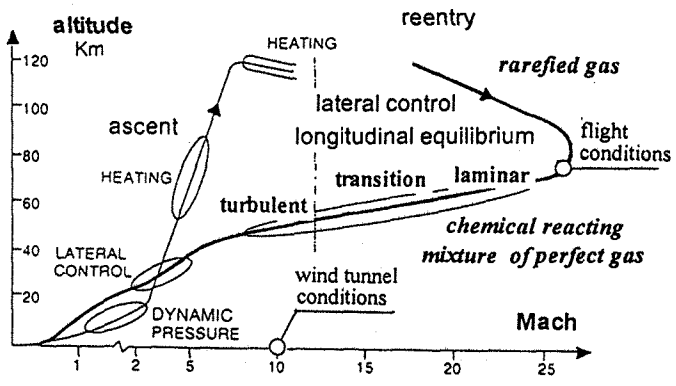

Fig.1 Flight envelope of HERMES (Ref.1).

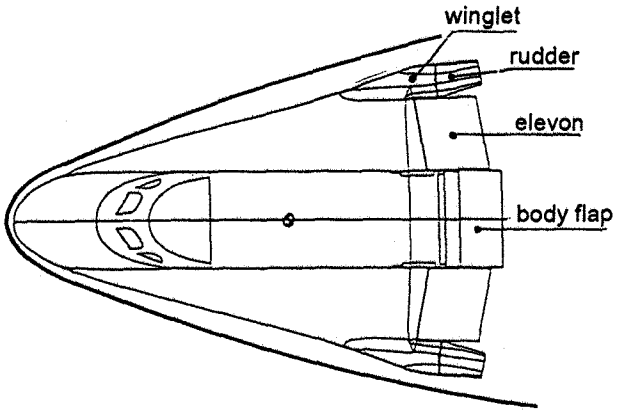

Fig.2 Geometry of HERMES (schematic).

In order to accurately simulate flight conditions in a wind tunnel, Reynolds number, Mach number and the thermochemical processes in the flow must be matched. Since that is not possible with present technology, strong penalties are introduced in the vehicle design due to the large uncertanties which account for the unknowns in extrapolation of wind tunnel data to free-flight. As example one should mention that during the first entry of the US Space Shuttle

Orbiter, the vehicle exhibited a larger nose-up pitching moment than predicted before flight, which caused the longitudinal control surface to deflect twice the amount thought necessary to achieve trimmed flight[2]. Today, due to the increased sophistication and robustness of numerical flow solvers and a several order of magnitude increase in computer power, computer simulation of hypersonic flow around 3D complex configurations can be used in some cases as transfer models[3],[4]. The typical approach is to assume that once wind tunnel flows obtained in cold or hot simulation facilities can be reproduced with computational tools, the extrapolation to the application for free-flight will be similarily successful.

In the present paper the efficiency of the longitudinal control surfaces of the HERMES spaceplane -shape 1.0- and the resulting heating due to deflection are analysed based on numerical solutions of the Navier-Stokes equations. The solutions are produced for free stream conditions corresponding both, cold wind tunnel tests at M_∞= 10 and a flight trajectory point at an altitude H=75km and M_∞= 25. The flow is computed as laminar, assuming for the low Mach number case calorically perfect gas and for the high Mach number case chemical reacting mixture of perfect gas. Computations are carried out for configurations without and with body flap and elevons deflected. The accuracy of the computed solutions is addressed by grid refinement studies and by comparing numerical results with available experimental data[5,6]. Also the importance of the viscous effects is shown by comparing the Navier-Stokes solutions with previous Euler solutions[7]. Furthermore, the effect of the geometry of the elevon on both, pitching moment efficiency and heating is studied for cambered and plain elevon geometries. The computed flow fields are simulated with the DLR Navier-Stokes code CEVCATS-RANS[8],[9].

2. Numerical experiment set-up

2.1 Solution Method

Two different upwind-biased spatial discretization of the inviscid fluxes can be selected on the CEVCATS-RANS code: a Total Variation Diminishing (TVD) formulation as proposed by Yee and Harten[10] and a modified version of the Advection Upstream Splitting Method (AUSM) according to Liou[11]. Viscous fluxes are taken into account only in the coordinate direction normal to the body surface (thin-layer approximation). They are discretized with central approximations[12]. The complete formulation of the numerical flux used for the viscous flows is given in[9]. The high-temperature effects on the thermodynamic and transport properties of air are implemented via vectorizable curve fits according to[13] which are based on Tannehill curves. An explicit five-stage time stepping scheme is used for advancing the solution in time. The CEVCATS-RANS code contains several convergence acceleration techniques to overcome the slow rate of convergence normally exhibited by explicit time stepping schemes for viscous flow computations. These techniques are: local time stepping, implicit residual smoothing and multigrid with full coarsening in all coordinate directions. Figure 3 displays typical convergence rates for the two flow conditions considered in this study. The root mean square of the derivative $\partial\rho/\partial t$ is reduced by four orders of magnitude for the low Mach number case and by three orders of magnitude within 250 multigrid cycles for the high Mach number case. Typical computer time on the DLR CRAY Y-MP to execute one multigrid cycle for one grid point is about 100μs on a single processor maschine.

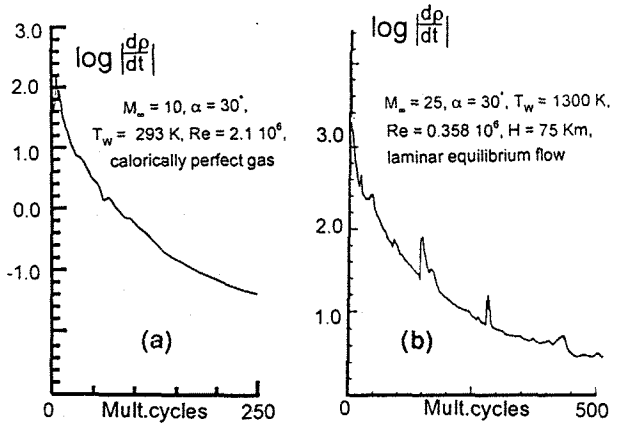

Fig.3 CEVCATS histories of convergence.
(a) M_∞=10 - (b) M_∞=25.

2.2 Configuration and grid strategy

The geometry used for the present study corresponds to the shape 1.0 of the European spaceplane HERMES. Since slide slip is not considered in this study, only half of the configuration is used in the computations. The surface geometry was constructed from CAD surfaces provided by ONERA. The numerical configuration differs slightly from

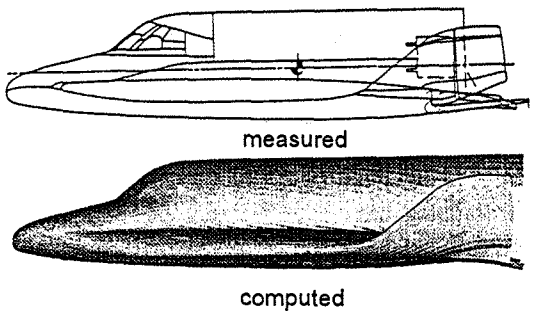

Fig.4 Experimental and computational configurations of HERMES vehicle.

the original defined by DASSAULT AVIATION, as one can observe from Fig.4. To facilitate surface and volume grid generation, the fuselage and the body flap extend up to the trailing edge of the wing. In addition, the elevon-winglet gaps have not been modelled. These alterations should not impact the information sought in this study. For the evaluation of forces and moments acting on the vehicle, the integral values of these quantities are corrected according to the neglected areas and moment arms. Furthermore, flow computation through slots for this configuration has been discussed in a previous paper [14]. For computational purposes two meshes are used for the present study: a global grid and a local grid. The first one corresponds to that of previous viscous results reported in[15] and is used for computations without deflection of the control surfaces. This mesh has a C-O topology and exhibits a polar singularity at the nose of the vehicle. It consists of 914225 grid points, where 64 cells are used in the normal direction to the body surface with aspect ratios for the near-wall cells in the order of 1000. The total size of the surface mesh consists of 144x96 cells. In order to allow flow computations with limited amount of core memory, the deflected control surfaces are treated as a separate entity. As described in[16] only a portion of the lower surface of the vehicle needs to be included when making deflected control surfaces calculations. The following procedure is used to define this portion of the lower surface, here designated as local grid (Fig.5):

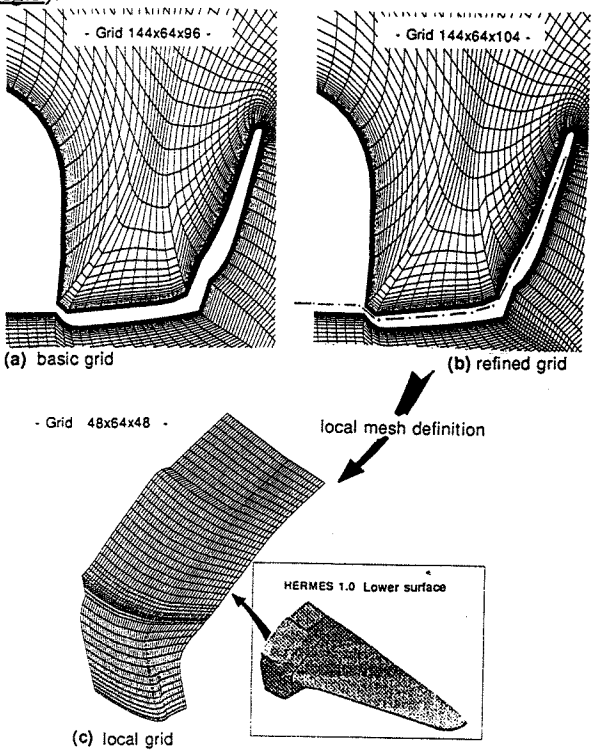

Fig.5 Local mesh generation procedure.
(a) basic mesh, (b) refined mesh, (c) local mesh.

- the starting point is the global grid previously described, which is locally refined at the outer edge of the elevon (Fig.5-a,b).
- Then, the controls are deflected by application of the grid processing tool[17].
- Finally, a computational box in the windward region of the controls is cut out as shown in Fig.5-c.

The grid size of this local mesh is 48 cells in streamwise direction, 64 cells normal to the wall and 48 cells in spanwise direction. Boundary conditions at the inflow boundaries of the local mesh are obtained by interpolation of the global solutions previously obtained. Information about the near-wall grid resolution for the local grid is given in Fig.6, where the distribution of the nondimensional grid spacing in normal direction y^+, is plotted. It is seen that y^+ is less than 1 over the complete surface for both flow conditions. Because local and global grids do not differ in the direction normal to the wall, Fig.6 is also representative of the near wall grid resolution of the global grid.

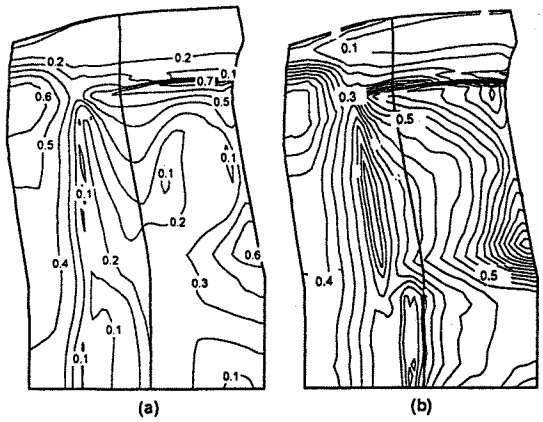

Fig.6 Near wall mesh resolution in terms of y^+.
(a) wind tunnel flow condition - (b) flight condition.

2.3 Grid convergence

Grid convergence studies for the two free stream flow conditions considered in the present study were performed using global and local grid refinement strategies. Figure 7 compares maximum heat flux values and flow structure for the M_∞=10 case, obtained on global grids of size 72x32x48 and 144x64x96 (the finest global grid used in this study). Although the coarse mesh does not resolve the peak values, the overall trend and flow structure of both solutions are similar. In a similar way, Fig.8 shows the effect on the resolution of heat fluxes and stream lines by increasing locally the number of grid points in spanwise direction at the outboard of the elevon of the local grid. The overall levels and trends of the heat fluxes of both solutions agree quite well. The local maximum of heating at the outboard lateral end

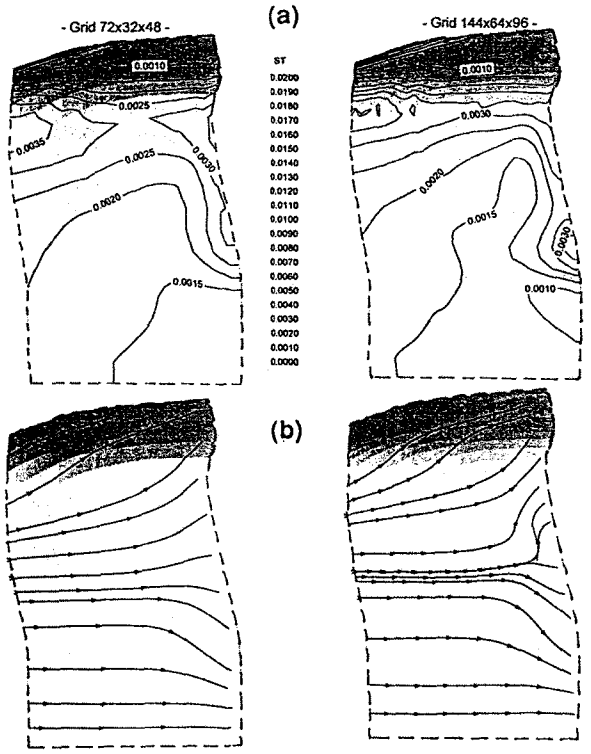

$M_\infty = 10, \alpha = 30^\circ, T_\infty = 52^\circ k, T_W = 293^\circ K, Re_L = 2.10\ 10^6, \delta = 0^\circ$
calorically perfect gas

Fig.7 Effects of global refinement on global grid.
(a)heat fluxes - (b) stream lines.

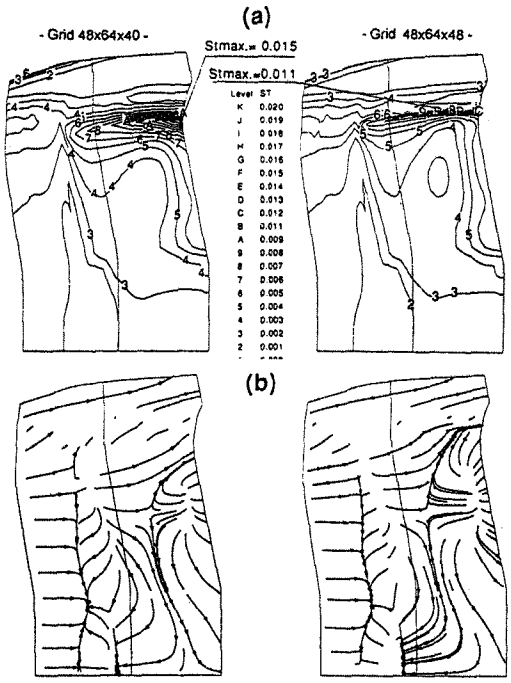

$M_\infty = 10, \alpha = 30^\circ, T_\infty = 52^\circ k, T_W = 293^\circ K, Re_L = 2.10\ 10^6, \delta = 10^\circ$
calorically perfect gas

Fig.8 Effects of local refinement on local grid.
(a)heat fluxes - (b) stream lines.

edge of the elevon is larger for the coarse mesh than for the fine mesh, indicating that this local peak of heating is partly a numeric response to the discontinuity of the grid metric at this point. Both solutions indicate the same flow structure, i.e. similar location of separation and attachment lines. On the coarse mesh solution, the separation area towards the outboard lateral end edge is reduced. Finally, Fig. 9 compares heat flux distributions and flow structure for the M_∞=25 case, obtained on local grids of size 24x32x24 and 48x64x48 (the finest local grid used in this study). The coarse mesh does not resolve the peak values and also is not able to resolve the shock induced boundary layer separation. Hence the levels and gradients of the computed heating on the coarse grid show, beyond the hinge line, some differences with respect to those computed on the fine mesh. For the part of the study that follows, only fine mesh results are discussed.

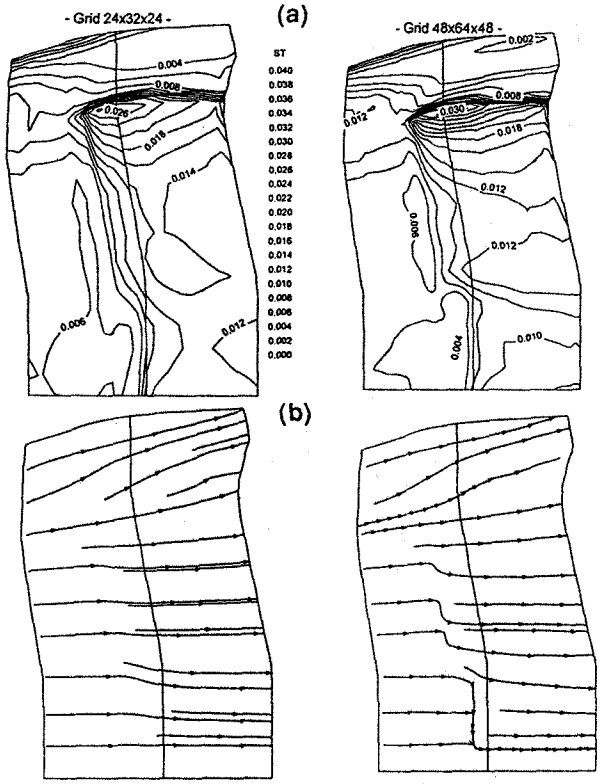

$M_\infty = 25, \alpha = 30^\circ, H = 75km, T_W = 1300^\circ K, Re_L = 0.358\ 10^6, \delta = 10^\circ$
laminar equilibrium flow

Fig.9 Effects of global refinement on local grid.
(a)heat fluxes - (b) stream lines.

3. Results and Discussion

3.1 Simulation of cold wind tunnel flow at M_∞=10

The reliability of the present study is assessed not only by grid refinement studies but also by comparing numerical solutions with available measurements. For the present chapter, computed solutions obtained at M_∞= 10 , Re = 2.1

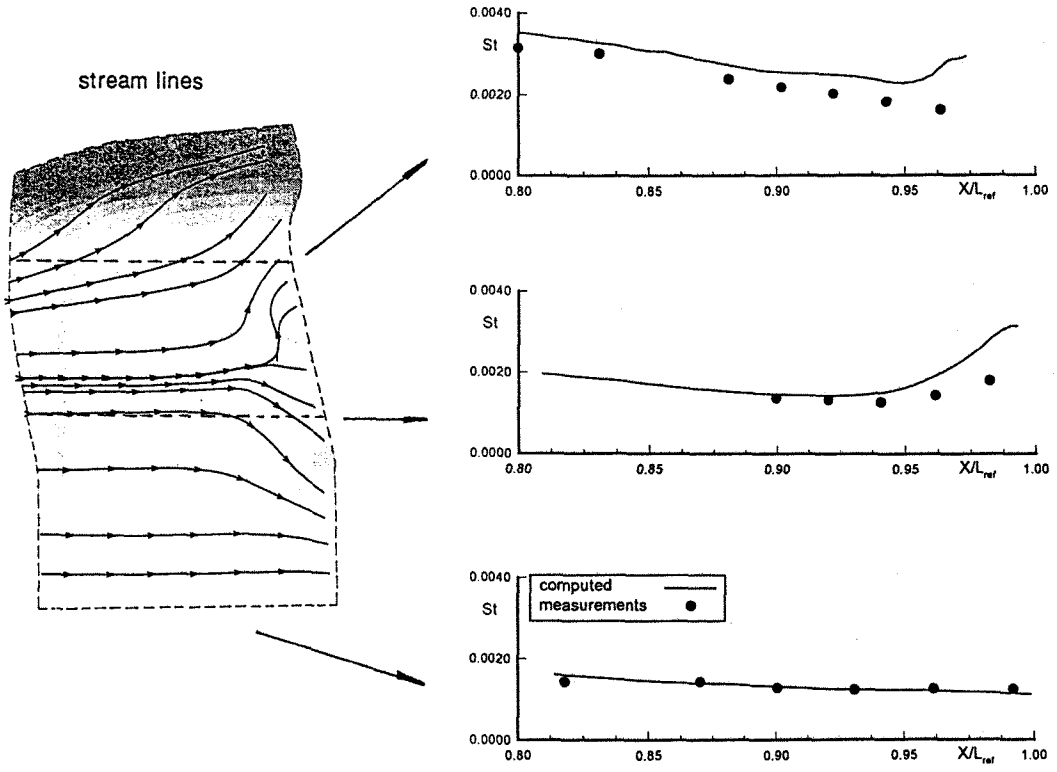

Fig.10 Experimental - numerical heat fluxes for the clean configuration.

10^6, T_W= 293°K , T_∞= 52°K , $\propto$= 30°, $\delta_{el.}=\delta_{bf}$= 0° and $\delta_{el.}=\delta_{bf}$= 10° are compared with experimental data obtained under these flow conditions. For the computations the hypothesis of calorically perfect gas is used and the state of the boundary layer is modelled as fully laminar. For the experiments the state of the boundary layer at the rear part of the configuration was not known. For the clean configuration case, Fig.10 shows a comparison of numerical and experimental heat fluxes in terms of the Stanton number, for three measured sections. Computed stream lines are also shown in the figure. In general the computed Stanton numbers agree rather well in level and trend with the experimental values. Only at the trailing edge of the elevon the numerical simulation shows higher values of heating due to the large stream line divergence computed there. In a same way, Fig.11 compares computed and measured heat fluxes for the configuration with deflected body flap and elevons. In general the computed Stanton numbers agree rather well in level and trend with the experimental values. Only at the symmetry plane (body flap surface), beyond the hinge line of the command a large missmatch occurs probably because in the wind tunnel transition occurs at reatachment. The computed efficiency of the control surfaces:

$C_{M,\delta=10} - C_{M,\delta=0} = -0.0255$ (where $C_{M,\delta=0} = 0.00826$)

compares rather well with the experimental[6] one:

$C_{M,\delta=10} - C_{M,\delta=0} = -0.0242$ (where $C_{M,\delta=0} \approx 0.01000$).

The differences in $C_{M,\delta=0}$ correspond to an elevon deflection angle of 0.7°.The correlation of the heat fluxes distribution with the flow structure given by the stream lines indicates that the heat fluxes are not only affected by local flow separations and reattachments, but also by the geometry of the elevon which leads to a peak of heating at the elevon trailing edge due to elevon camber, and also by flow divergence which generates peak heat fluxes towards the elevon lateral end edges. Due to the deflection of the control surfaces, an oblique shock is induced which produces boundary layer separation ahead and along the hinge line of the control surfaces. At the body flap the flow separates for a second time and reattaches close to the trailing edge. Also, the elevon shows a second flow separation which comprises about 50% of its area. The loss in flap efficiency

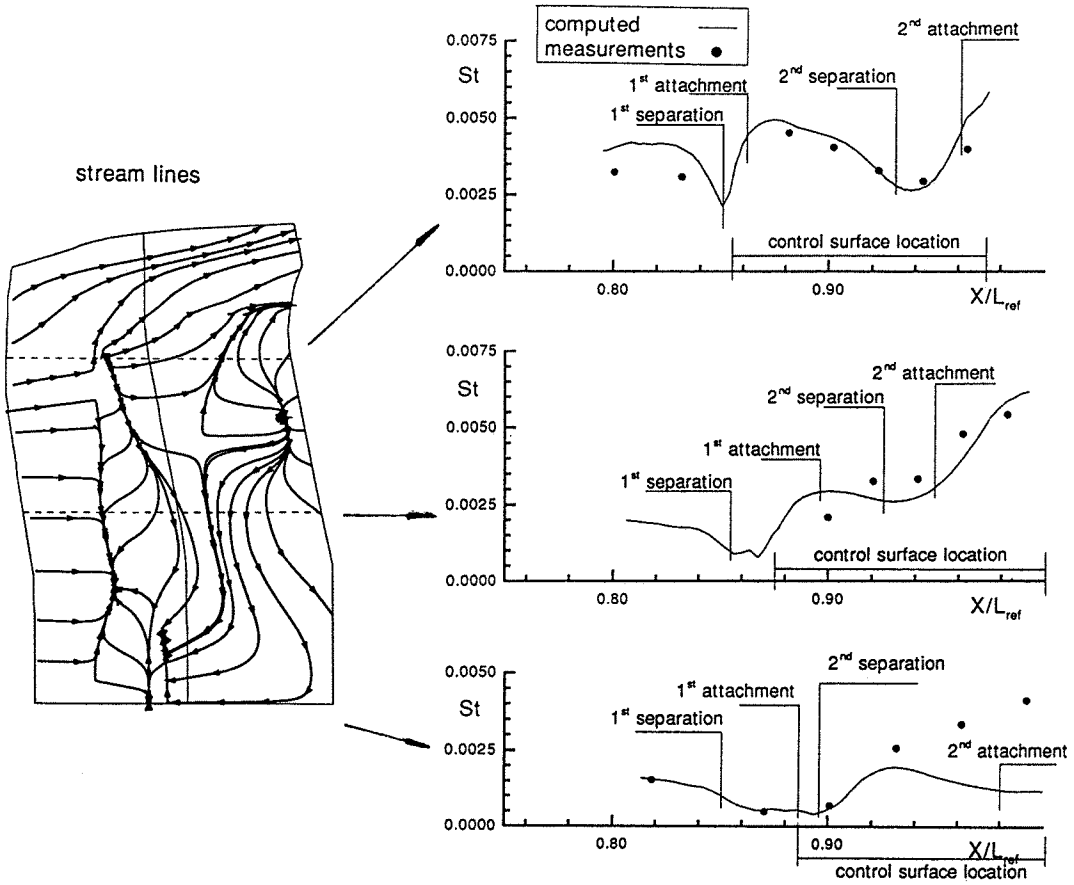

Fig.11 Experimental - numerical heat fluxes for the configuration with deflected control surfaces.

due to viscous interaction is evaluated by comparing the here computed pitching moment coefficients with previous values obtained by the numerical solution of the Euler equations:

$\Delta C_{M\ viscous} = C_{M,\delta=10} - C_{M,\delta=0} = -0.0255$ ($C_{M,\delta=0} = 0.00826$)

$\Delta C_{M\ inviscid} = C_{M,\delta=10} - C_{M,\delta=0} = -0.0265$ ($C_{M,\delta=0} = 0.0086$).

It turns out that for M_∞=10 the viscous effects introduce only minor losses on control surface efficiency (app.4%).

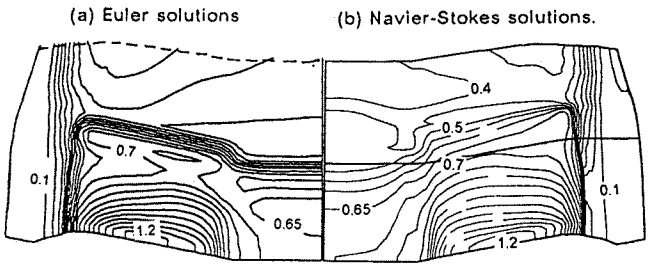

M∞ = 10, α = 30°, T∞ = 52°k, TW = 293°K, ReL = 2.10 10^6, δ = 10°

Fig.12 Iso-Cp on the windward side rear part of the configuration with deflected control surfaces.

Computed inviscid and viscous pressure distributions acting on the control surfaces for the case with deflected control surfaces are shown in Fig.12. In general both solutions show similar trends. That means the pressures acting on this portion of the configuration are almost boundary layer independent. At the hinge lines of the deflected controls an oblique shock induces a pressure rise which is smeared in the viscous case due to the boundary layer. Figure 13

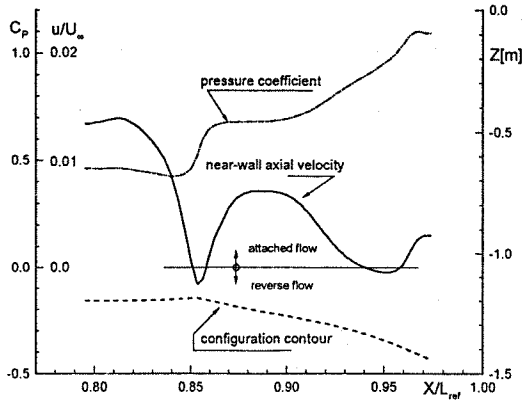

Fig.13 Shock-wave / boundary layer interaction.

shows details of this shock-wave / boundary layer interaction for a plane normal to the configuration windward side, parallel to the symmetry plane at the position of the so-called external elevon plane. The large pressure rise across the shock wave causes the boundary layer separate. Behind the location where the flow reattaches, the increase on elevon camber produces a new flow separation. Finally, close to the trailing edge the flow reattaches to the surface which is probably influenced by the boundary condition used on the numerical method.

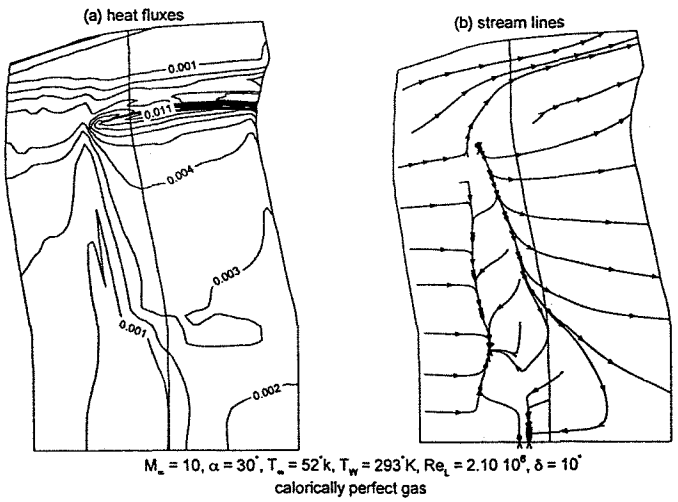

Fig.14 Plain elevon, deflected configuration, at M_∞=10.
(a) heat fluxes - (b) stream lines.

In order to assess the sensitivity of the heating due to elevon camber, a configuration with plain elevons is also tested. Computed stream lines and heat fluxes for this configuration is shown on Fig.14. The new configuration also indicates shock induced boundary layer separation at the hinge line of the control surfaces, but the extended flow separation area exhibited by the camberd elevon is removed. The plain elevon configuration shows a plateau shape for the heat fluxes resulting at the rear part of the control surfaces. Both elevon configurations exhibit similar levels of heat fluxes up to the location of the control surfaces (Fig.15). On the body flap as well as on first half of the elevon, the plain elevon configuration shows slightly larger values of heat fluxes, but the rise of the heat fluxes at the trailing edge of the cambered elevon is removed with the new elevon configuration. A similar trend was observed experimentally, using an elevon with less camber instead of a plain elevon.

3.2 Simulation of a flight trajectory point at M_∞=25

Since at the present, high temperature effects can not be fully simulated in ground-based facilities, the analysis of the aerodynamics characteristics of the longitudinal control surfaces of the spaceplane HERMES at flight conditions could be done only with numerical simulation. For the

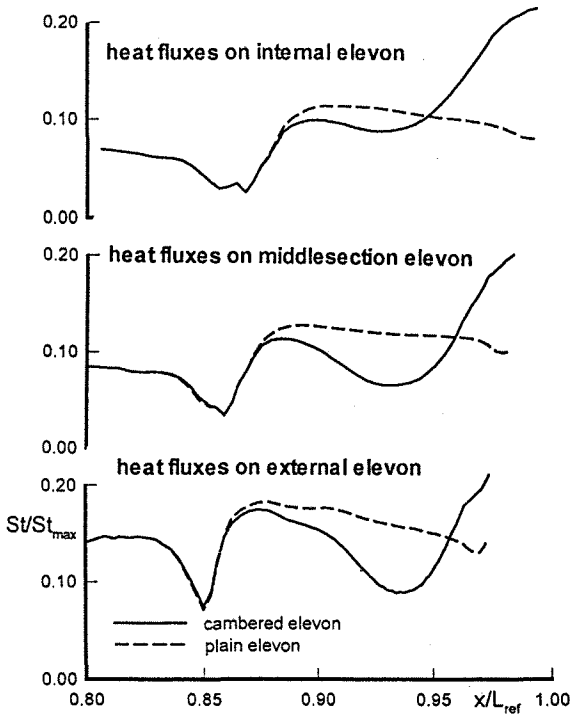

Fig.15 Plain vs. cambered elevon heat fluxes at M_∞=10.

present chapter, the free stream flow condition adopted corresponds to a flight trajectory point at an altitude of H = 75 km , M_∞= 25 , α= 30°, Re = 0.358 10^6, T_W= 1300°K . The flow is modelled as fully laminar, assuming air in thermo-chemical equilibrium. . Figures 16 shows computed stream lines and heat fluxes for the configuration with cambered elevon with deflected control surfaces. In comparison with the results obtained at M_∞=10 (Figs. 8 and 11), it turns out that for M_∞=25 the flow separation at the control surfaces is strongly reduced. A comparison of the computed heat fluxes indicate almost a factor four between both free stream flow conditions. Even though the flow divergence

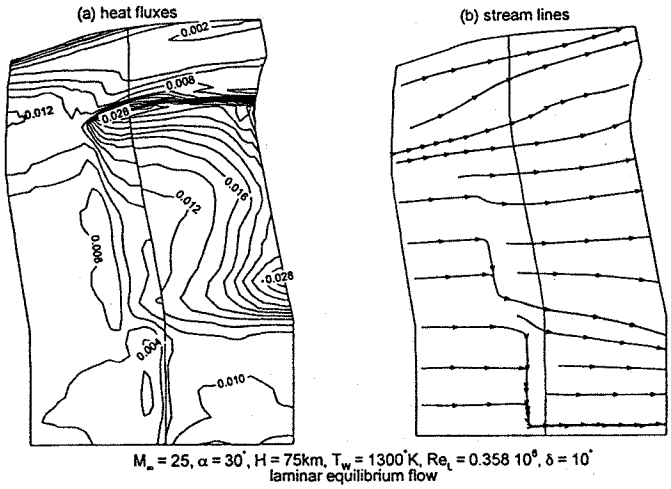

Fig.16 Cambered elevon - deflected conf. at M_∞=25.
(a) heat fluxes - (b) stream lines.

of the elevon boundary layer seems to be weaker at flight conditions, it has an strong effect on the heat fluxes distribution. Figure 17 shows that there are markable concentrations of heating at the outboard and inboard end edges of the cambered elevon,

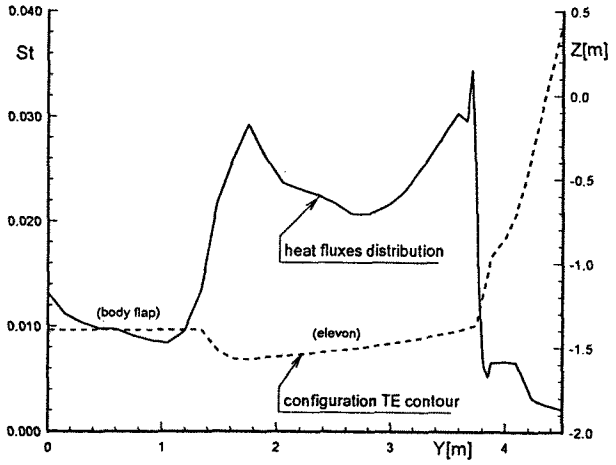

Fig.17 Heat fluxes along cambered elevon TE at M_∞=25.

where the local values exceeded in about 50% the heat flux values acting on the middle of the trailing edge. The computed viscous efficiency of the control surfaces:

$C_{M,\delta=10} - C_{M,\delta=0} = -0.0352$ (where $C_{M,\delta=0} = 0.0116$)

compares quite good with that obtained previously by the numerical solution of the Euler equations:

$C_{M,\delta=10} - C_{M,\delta=0} = -0.0354$ (where $C_{M,\delta=0} \approx 0.0132$), which means that the control surfaces efficiency obtained for the present viscous simulation is only marginally smaller than for the inviscid flow (less than 0.5%). The comparison of the above pitching moment values with those obtained for the M_∞=10 case shows that the control surface efficiency is as much as 38% greater for flight conditions than for wind tunnel flow conditions. Of particular interest is the increment in nose-up pitching moment for the clean configuration. This problem is known as "pitching moment anomaly" in the history of the US Space Shuttle Orbiter development. It has been recently demonstrated[18] that the anomaly is caused by high temperature effects. At flight condition, the primary high temperature effect on aerodynamic characteristics is a lowering of the specific heat ratio (γ) within the shock layer. This fact produces a greater degree of flow expansion compared to the case γ=1.4 (perfect gas) and a corresponding reduction in surface pressures over the aft region of the vehicle, resulting in a nose-up increment for the flight clean configuration pitching moment. This effect is also found in the present numerical simulation.

Finally, Fig.18 shows results for the plain elevon configuration. At flight conditions, this configuration exhibits a quasi 2-D flow structure along the whole elevon and a plateau-type shape of heat fluxes acting on the control surfaces. As like as for the M_∞=10 case, the configuration with plain elevon shows approximately 50% less heating at the trailing edge of the elevon than the configuration with cambered control surface.

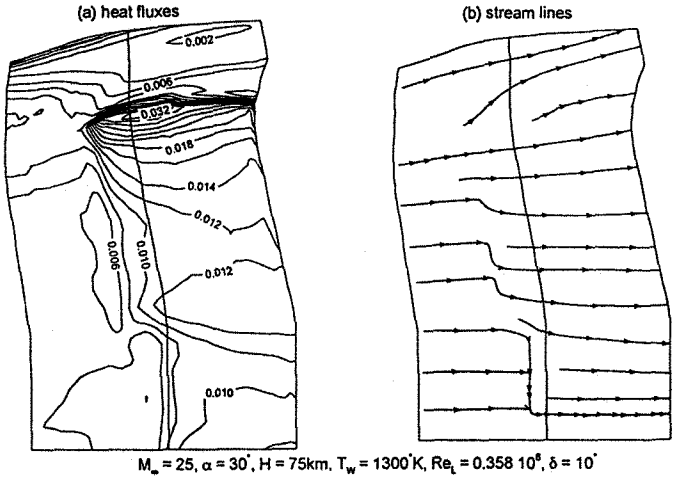

Fig.18 Plain elevon - deflected configuration at M_∞=25.
(a) heat fluxes - (b) stream lines.

3.3 Control surface efficiency versus control heating

Figures 19 and 20 display the peak heating on the control surfaces versus the pitching moment obtained with control deflection, for both free stream flow conditions and both elevon geometries. In Fig.19 the values of heat fluxes exhibited on the first third of the elevon midchord are used, while the reference conditions (index clean) are taken at the first third of the control surface for the clean configuration with plain elevons. For M_∞=10, the cambered elevon configuration shows a lower level of heat fluxes than the plain one, due to the flow separation on the cambered elevon.

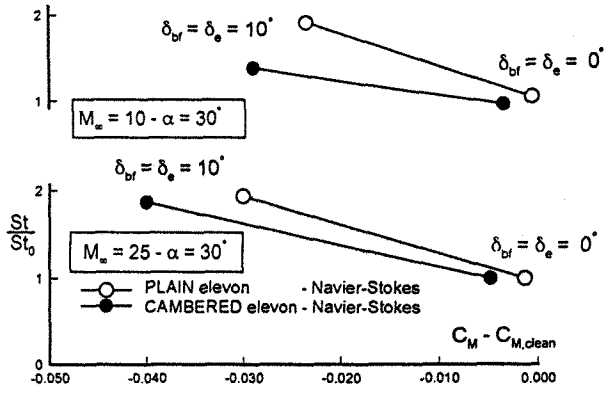

Fig.19 Influence of elevon geometry and of pitching moment on heat fluxes on elevon first third.

Since at M_∞=25 the cambered elevon exhibites a similar flow structure than the plain one, there are only small differences on the peak heating acting on the first third of the elevons. In Fig.20 the maximum values of heat fluxes exhibited on the midsection of each elevon are used, while the reference conditions (index clean) are taken at the trailing edge of the control surface for the clean configuration with plain elevons. Euler results corrected according to a semiempirical correlations for a 2-D ramp are also included. The results indicate that the semiempirical approach is usefull as long as the geometries do not exhibit curvatures in streamwise direction. While the plain elevon configuration exhibits similar values of heat fluxes at the trailing edge as compared to the first third of the control surface, the cambered elevon shows a greater level of heat fluxes in comparison with the corresponding values at the first third of the elevon midchord. Also, asuming a linear variation of maximum heat fluxes for command deflections between δ= 0° and δ= 10°, the plain elevon configuration not only exhibits a lower level of heating but also a lower rate of heat flux increases with deflection angle (about only 65% of the rate for the cambered configuration) for both flow regimes.

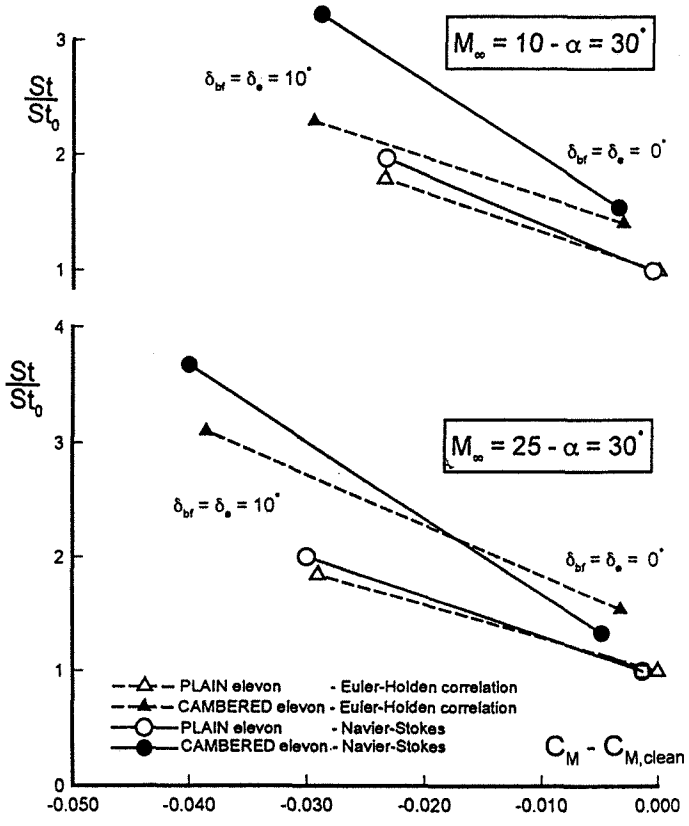

Fig.20 Influence of elevon geometry and of pitching moment on heat fluxes on elevon trailing edge.

4. Conclusions

In the present study Navier-Stokes solutions are analysed for the HERMES reentry vehicle at free stream conditions corresponding both, cold wind tunnel tests at M_∞= 10 and a flight trajectory point at M_∞= 25 . The flow was computed as laminar, assuming for the low Mach number case calorically perfect gas. The high-temperature effects on thermodynamic and transport properties are modelled by assuming air in thermochemical equilibrium. The reentry vehicle modeled in this study is equipped with body flap and elevons as control surfaces. Computations are carried out for $\delta_{el.}$= $\delta_{bf.}$= 10°. The accuracy of the computed solutions is addressed by grid refinement studies and by comparing numerical results with available experimental data. Also the importance of the viscous effects is shown by comparing the Navier-Stokes solutions with Euler solutions. Furthermore, the effect of the geometry of the elevon on both, elevon efficiency and heating is studied for two types of elevon geometry: cambered and plain. The computed flow fields are simulated with the DLR Navier-Stokes code CEVCATS-RANS. The results obtained for M_∞= 10 for the cambered elevon configuration exhibit large areas of separated flow, especially at the hinge line of the deflected controls. The local distributions of wall heat fluxes are in good agreement with measured data. By changing to flight flow conditions the separation areas are greatly reduced but there remain significant 3-D effects on the heat fluxes. These effects are traced to flow divergence at the lateral edges of the cambered elevon and they are larger for M_∞= 25 than for wind tunnel conditions. The plain elevon configuration shows about 50% less heating than the cambered one for the range of deflections investigated here, even if one takes into account the larger deflection angles of the plain elevon needed to achieve equilibrium in pitching moment. At wind tunnel flow conditions the plain elevon does not exhibit flow separation at the elevon itself and also the rise of heat fluxes at the trailing edge of the elevon is suppressed. At free flight conditions, the plain elevon exhibits a quasi 2-D flow along the whole command and a plateau shape for the heat fluxes. Comparison of the computed pitching moment from Euler and Navier-Stokes results for both elevon configurations indicate small losses of control surfaces efficiency due to viscous interaction. However, the high-temperature effects on elevon efficiency can not be neglected. Having in mind the limitations of the flow model used, the present study demonstrates the ability of computational fluid dynamics to simulates critical reentry flow phenomena.

Acknowledgement

The present investigations were done under contract ESA-CNES Nr.9628-91-F-BM, "DLR Technical Assistence to

CNES concerning HERMES Aerothermodynamics" and monitored by G. Durand, CNES-Toulouse, France.

5. References

1. Isakeit D.: *High Temperature Aspects of the European Hermes Programs.* Third Aerospace Symposium, Eds. H. Oertel - H. Körner, Springer-Verlag (1991), pp. 83 to 102.

2. *Shuttle Performance: Lessons Learned.* NASA CP-2283 (1983).

3. Griffith B. J., Maus J. R. and Pouts C.: *Explanation of The Hypersonic Longitudinal Stability Problem - Lesson Learned.* NASA CP-2283 (1983).

4. Weilmuenster K.J., Gnoffo P.A. and Greene F.A..: *Navier-Stokes Simulations of the Shuttle Orbiter Aerodynamic Characteristics with Emphasis on Pitch Trim and Body Flap.* AIAA 93-2814 (1993).

5. Stojanowski, M.: *Hermes 1.0 - Mesure des flux thermiques avec thermocouples sur la maquette no. 3041 au 1/40 dans la soufflerie S4MA à Mach 10.* H.RE.1.1114.AMD (1992).

6. Stojanowski, M.: *Hermes 1.0 au 1/40 à S4MA - Identification aérodynamique à Mach 10 avec la maquette no. 3026.* H.RE.1.1106.AMD (1992).

7. Poirier D., Findling A. and Radespiel R.: *Longitudinal Control Efficiency of Hermes(1.0) with Straight Elevons at High Mach Numbers*. DLR-IB 129-91/28 (1991).

8. Schone J., Kroll N. and Streit Th.: *Steps Towards an Efficient and Accurate Method for Solving The Euler Equations Around a Reentry Configuration at Supersonic and Hypersonic Speeds.* Proceedings of The European Symposium on Hypersonic. ESTEC-ESA, SP-318 (1991), pp.115 to 120.

9. Kroll N. and Radespiel R.: *An Improved Flux Vector Split Discretization Scheme for Viscous Flows.* DLR-FB 93-53 (1993).

10. Yee H.C. and Harten A.: *Implicit TVD Schemes for Hypersonic Conservation Laws in Curvilinear Coordinates.* AIAA Journal 25 (1987), pp.266-274.

11. Liou M.S. and Steffen C.J.: *A New Flux Splitting Scheme.* NASA TM 104404 (1991).

12. Radespiel R., Rossow C.-C. and Swanson R.C..: *An Efficient Cell-Vertex Multigrid Scheme for Threedimensional Navier-Stokes Equations.* AIAA Journal, Vol.28, No.8, pp. 1464-1472 (1990).

13. Mundt Ch., Keraus R. and Fischer J.: *New Accurate Vectorized Approximations of State Surfaces for The Thermodynamic and Transport Properties of Equilibrium Air.* ZfW 15 (1991), pp.179-184

14. Herrmann U., Radespiel R. and Longo J.M.A.: *Critical Flow Phenomena on the Winglet of Winged Reentry Vehicles.* AIAA 94-0629 (1994).

15. Verant J.L., Radespiel R. and Hugues E.: *Development of Three-Dimensional Real Gas Navier-Stokes and Parabolized Navier-Stokes Codes. Application to Hermes Space Shuttle.* AIAA 93-0675 (1993).

16. Herrmann U. and Poirier D.: *Interpolation Procedure Allowing Local 3D Navier-Stokes Computations on Refined Meshes.* DLR-IB 129-93/5 (1993).

17. Poirier D.:*Grid Processor for The Simulation of Control Surface Deflection.* DLR-IB 129-91/07 (1991).

18. Brauckmann G.J., Paulson Jr. J.W. and Weilmuenster K.J.: *Experimental and Computational Analysis of the Space Shuttle Orbiter Hypersonic "Pitch-Up Anomaly".* AIAA 94-0632 (1994).